Synthesis and Rate Performance of Monolithic Macroporous Carbon Electrodes for Lithium-Ion Secondary Batteries**

By *Kyu T. Lee*, *Justin C. Lytle, Nicholas S. Ergang*, *Seung M. Oh*, and *Andreas Stein**

Three-dimensionally ordered macroporous (3DOM) materials are composed of well-interconnected pore and wall structures with wall thicknesses of a few tens of nanometers. These characteristics can be applied to enhance the rate performance of lithium-ion secondary batteries. 3DOM monoliths of hard carbon have been synthesized via a resorcinol-formaldehyde sol–gel process using poly(methyl methacrylate) colloidal-crystal templates, and the rate performance of 3DOM carbon electrodes for lithium-ion secondary batteries has been evaluated. The advantages of monolithic 3DOM carbon electrodes are: 1) solid-state diffusion lengths for lithium ions of the order of a few tens of nanometers, 2) a large number of active sites for charge-transfer reactions because of the material's high surface area, 3) reasonable electrical conductivity of 3DOM carbon due to a well-interconnected wall structure, 4) high ionic conductivity of the electrolyte within the 3DOM carbon matrix, and 5) no need for a binder and/or a conducting agent. These factors lead to significantly improved rate performance compared to a similar but non-templated carbon electrode and compared to an electrode prepared from spherical carbon with binder. To increase the energy density of 3DOM carbon, tin oxide nanoparticles have been coated on the surface of 3DOM carbon by thermal decomposition of tin sulfate, because the specific capacity of tin oxide is larger than that of carbon. The initial specific capacity of SnO_2-coated 3DOM carbon increases compared to that of 3DOM carbon, resulting in a higher energy density of the modified 3DOM carbon. However, the specific capacity decreases as cycling proceeds, apparently because lithium–tin alloy nanoparticles were detached from the carbon support by volume changes during charge–discharge processes. The rate performance of SnO_2-coated 3DOM carbon is improved compared to 3DOM carbon.

1. Introduction

Lithium-ion secondary batteries are promising candidates for sources to power electric vehicles and microelectronic devices.[1] However, many applications would benefit from higher energy and power densities than are currently achievable with lithium-ion batteries. One approach to meet this need has been to increase specific capacities of anode materials by replacing carbon-based anodes with elements or compounds that alloy with lithium (e.g., Sn, Sb, Si, or Ge), which have much larger specific capacities than commercial graphite materials (Sn: 990 mA h g^{-1}, SnO_2: 780 mA h g^{-1}, Sb: 660 mA h g^{-1}, Si: 4200 mA h g^{-1}, Ge: 1600 mA h g^{-1}, compared to 372 mA h g^{-1} for graphite).[2–9] Also, nanostructured materials have been investigated to improve high rate performance related to power density.[10–19] In general, the rate-limiting step of lithium-ion secondary batteries is known to be solid-state diffusion of lithium ions.[20,21] Hence, much research has focused on decreasing particle sizes of electrode materials.[22–24]

During discharge of lithium-ion secondary batteries, lithium ions move from anode to cathode through an electrolyte. Therefore, even though solid-state diffusion of lithium ions within anode and cathode materials is usually the rate-limiting step, the rate is also affected by charge-transfer reactions at the electrode surfaces and by lithium-ion conduction in the electrolyte.[25,26] All three processes should be considered in the design of new electrodes to improve rate capability. In the present work, an electrode architecture based on inverse-opal structures[27] was evaluated to address issues of rate performance. In particular, we report the synthesis and electrochemical characterization of monolithic, three-dimensionally ordered macroporous (3DOM) hard carbon[28] anodes and modifications of these anodes with SnO_2 surface coatings. Similar 3DOM structures of V_2O_5 and SnO_2 compositions have recently been reported.[16,29,30]

3DOM materials are inverse replicas of their colloidal-crystal templates, possessing solid nanostructures where voids between close-packed template spheres once existed. They are composed of nanometer-sized walls that surround interconnected close-packed spherical voids with sub-micrometer diameters. The wall thicknesses of 3DOM materials are typically less than 50 nm; this is compared to particle sizes of a few micrometers in commercial lithium-ion secondary battery materi-

[*] Prof. A. Stein, J. C. Lytle, N. S. Ergang
Department of Chemistry, University of Minnesota
Minneapolis, Minnesota 55455 (USA)
E-mail: stein@chem.umn.edu
K. T. Lee, Prof. S. M. Oh
School of Chemical Engineering and
Research Center for Energy Conversion & Storage
Seoul National University, Seoul 151–744 (Korea)

[**] This research was supported by the Brain-Korea 21 program between Seoul National University and the University of Minnesota, by the Office of Naval Research (grant number N00014-01-1-0810, subcontracted from NWU), and in part by the U.S. Army Research Laboratory and the U.S. Army research office (DAAD 19-01-1-0512), the MRSEC program of the NSF (DMR-0212302), and KOSEF through the Research Center for Energy Conversion and Storage. We thank Professor W. H. Smyrl for providing access to his electrochemical testing facility.

 DOI: 10.1002/adfm.200400186

als. Hence, solid-state diffusion lengths for lithium ions in 3DOM materials are much shorter than in commercial particles. Furthermore, 3DOM materials can benefit charge-transfer reaction rates because of the relatively large surface areas obtained with this architecture (10–400 $m^2 g^{-1}$ and higher).[31,32]

3DOM carbon, in particular, provides several advantages in battery applications. It can be prepared in monolithic form and used as an active electrode without additional binder or conducting agents. Its well-interconnected wall structure can provide a continuous electronic pathway, yielding an electrical conductivity of reasonable magnitude for Li-ion batteries. In comparison, composite electrodes prepared from powders, conducting agents, and binder can experience poor electrochemical performance when the electrode thickness exceeds a few hundred micrometers, due to low electrical conductivity and poor ionic access of the electrolyte to the active particles. Composite electrodes composed of nanoparticles as active material can, in principle, possess high rate capabilities due to short ion-diffusion pathlengths. In practice, the high surface area of nanoparticles requires additional binder and conducting agents to provide electronic connectivity between the particles, resulting in lower energy densities. Monolithic 3DOM carbon electrodes can be thicker (400–900 μm in this study), because their sufficient electrical conductivity and well-interconnected macroporous structure facilitate the conduction of lithium ions in the electrolyte to the easily accessible 3DOM pore surfaces. With thicker electrodes, the fraction of required current collector material is reduced, so that the energy density of a cell can be improved.

Although 3DOM materials possess relatively large specific energies and specific powers, an inherent disadvantage of these materials is their low volumetric energy density because of the high porosity of the structure (> 74 %). To improve the energy density of 3DOM carbon, we coated SnO_2 on the surface of 3DOM carbon, because SnO_2 has a higher specific capacity than carbon. The electrochemical characteristics of 3DOM carbon, non-templated carbon, carbon sphere electrodes, and SnO_2-coated carbon were compared.

This work is intended to complement the numerous studies of carbonaceous materials by exploring the influence of an inverse-opal structure on the electrochemical properties of carbon. It is important to note that the purpose of this work was not to find the best form of carbon, which was a factor limited by our synthesis. Carbon electrode materials are commonly organized into three major structural classes: graphitic carbons, soft (graphitizable) carbons, and hard (non-graphitizable) carbons. Dahn and co-workers have also proposed a sub-category for both soft and hard carbons that accounts for the unique electrochemical contributions of hydrogen-containing carbons.[33–35] Each form of carbon exhibits unique electrical and electrochemical properties that stem from differences in crystallinity, porosity, particle morphology, and chemical composition.[33,36] For example, graphitic carbons are composed of lamellar planes of sp^2-hybridized C_6 fused rings (i.e., graphene sheets) that can reversibly accommodate mobile species. As a result of their distinctive structure, graphitic carbons exhibit large electrical conductivities parallel to their graphene layers (of the order of 10^2–10^3 $S cm^{-1}$),[37–40] a theoretical specific capacity of 372 mA h g^{-1} for Li ions, and good cycling stability.[41] In contrast, the structure of hard carbons is often compared to a "house of cards" built of randomly arranged graphene sheets.[34] It is thought that Li ions can adsorb to both faces of the sheets and can occupy the micropores found between them, permitting specific capacities of ca. 500–800 mA h g^{-1}. However, hard carbons typically suffer from large irreversible capacities due to the formation of solid–electrolyte interface (SEI) layers and reactions of Li with surface functional groups and/or adsorbed molecules.[41] They also experience cycling hysteresis when Li-ion insertion occurs at a significantly different potential than de-insertion, causing large reductions in the working potentials of batteries. Phenolic resins, such as the resorcinol-formaldehyde (RF) precursor used in this work, produce hydrogen-containing hard carbons when heated between 500–1000 °C under an inert atmosphere.[33,42–47] They are relatively cost-efficient to produce, and have high pyrolysis yields. With the electrochemical limitations of hard carbons in mind, RF carbon served as a useful model material to compare the effects of electrode structure on a submicrometer scale.

2. Results and Discussion

2.1. Synthesis and Structure of 3DOM Carbon

Colloidal crystals of close-packed poly(methyl methacrylate) (PMMA) spheres, formed by gravitational settling, were used as templates for 3DOM carbon (Fig. 1a). Thermal processing of the PMMA/RF polymer composite in an inert atmosphere produced a well-ordered skeleton of hard carbon and resulted in removal of the template. Even though a large amount of shrinkage was observed after carbonization of the RF polymer, millimeter-sized 3DOM carbon monoliths with regular arrays of interconnected macropores were obtained (Figs. 1b–d). The dimensions of 3DOM carbon monoliths depended on the size of the colloidal PMMA crystal template, typical values being ca. 0.5 cm × 0.5–2.0 cm × 2.0 cm. The thicknesses of the electrodes were controlled from 300 μm to a few millimeters by polishing. Based on estimates from SEM images of 3DOM carbon monoliths, an average pore spacing of 298 nm was obtained from PMMA spheres with an average diameter of 408 nm (sample C1) and a pore spacing of 353 nm from 469 nm PMMA spheres (sample C2). Pore spacings were estimated from edge-to-edge measurements of the hemispherical dimples on the surface of 3DOM samples, which correspond to the spherical voids of the inverse-opal geometry. Voids are connected through pore windows, which appear in the scanning electron microscopy (SEM) images as dark circles or ellipses ≤ 100 nm in diameter. The estimated average wall thickness at the narrow points of the carbon wall was 10 nm for both samples (see Table 1). A further testament to the well-ordered, homogeneous structure of monolithic 3DOM carbon pieces (sample C1) was their opalescent green appearance (Fig. 2).

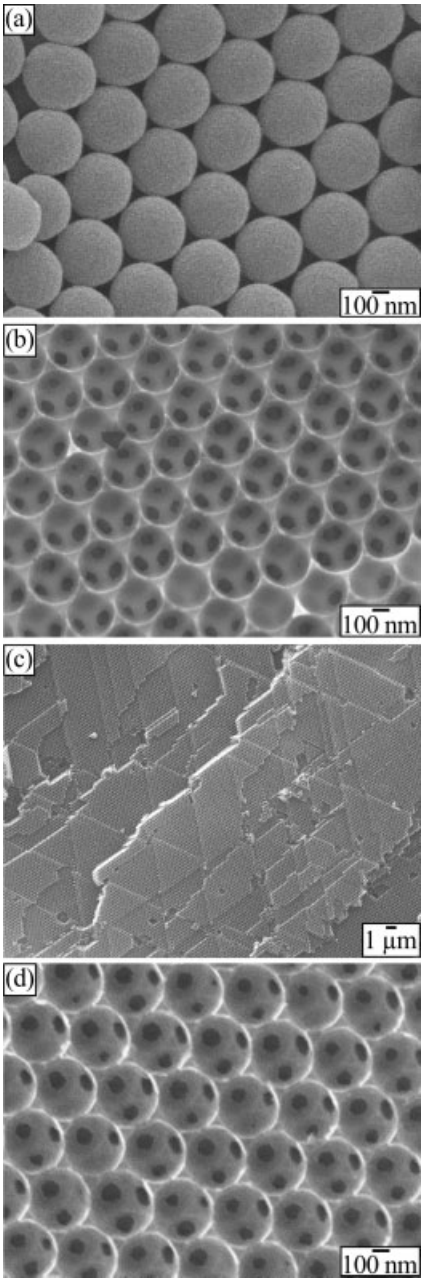

Figure 1. SEM images of a) the PMMA colloidal-crystal template used to prepare 3DOM carbon sample C1, b) 3DOM carbon sample C1, c) 3DOM carbon sample C1 at lower magnification to show the long-range periodicity of the sample, and d) 3DOM carbon sample C2.

Opalescence arises from diffraction of visible light by the periodic structure of the material with repeat distances of the order of the wavelength of light.[48,49] The green color correlated with a broad stop band in the UV-vis spectrum at 529 nm (Fig. 3). The bulk density of the 3DOM carbon monolith (sample C1) was 0.36 g cm^{-3}, and the mechanical strength of the macroporous solid was sufficient for use as an electrode in the sandwich configuration shown in Figure 4. 3DOM carbon yielded an X-ray diffraction (XRD) pattern with broad reflections at ca. 22° and 44° 2θ (data not shown), which is similar to XRD data reported for phenolic resin carbons.[45] These reflections are thought to correspond to the (002) and (100) reflections of non-parallel graphene sheets, respectively.

Table 1. Critical dimensions of 3DOM carbon and tin oxide-modified 3DOM carbon electrodes.

	Pore spacing [a] [nm]	Pore size [a] [nm]	Wall thickness [a] [nm]	Electrode thickness [b] [μm]
C1	298 ± 5	285 ± 11	10 ± 2	402
C2	353 ± 4	341 ± 8	10 ± 2	439
C3 [c]	298 ± 5	285 ± 11	10 ± 2	751
SnC1 [c]	305 ± 7	273 ± 5	27 ± 5	888
SnC2 [c]	305 ± 7	273 ± 5	27 ± 5	432

[a] Estimated from SEM images; errors are based on one standard deviation σ^{n-1} for ten measurements. [b] Measured with a micrometer. The thickness of the electrode prepared from spherical carbon (diameter: 104 ± 17 nm) was 191 μm. [c] Prepared from the same batch as sample C1 using PMMA spheres with 408 ± 6 nm diameters. The diameter of PMMA spheres used to template C2 was 469 ± 12 nm.

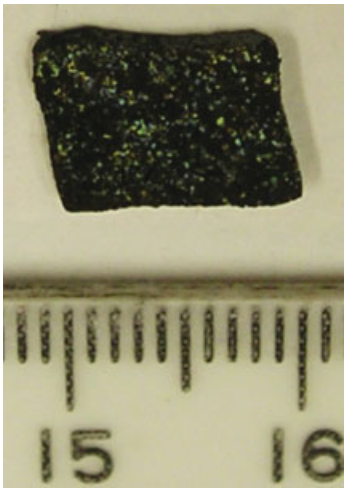

Figure 2. Photograph of monolithic 3DOM carbon electrode (C1) with a length of ca. 1 cm.■was rotated so the numbers appear upright■

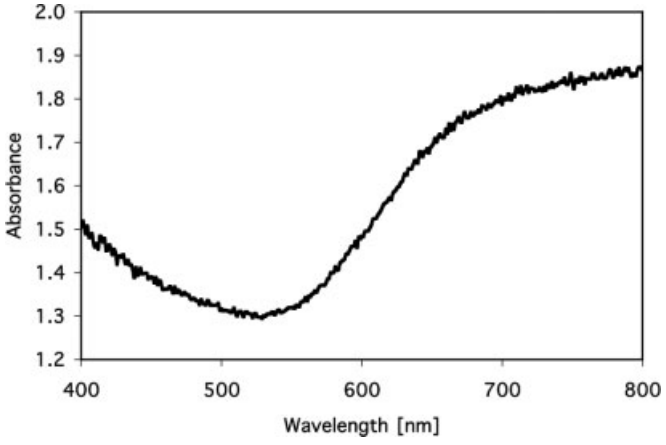

Figure 3. UV-vis reflectance spectrum of monolithic 3DOM carbon electrode (C1).

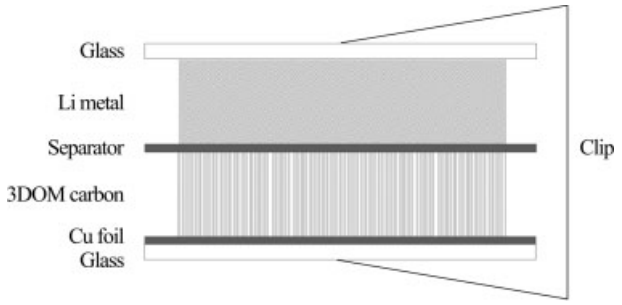

Figure 4. Diagram of the electrode assembly incorporating the 3DOM carbon anode. A similar assembly was used for the non-templated carbon sample and an anode prepared with carbon spheres.

Nitrogen-sorption measurements of 3DOM carbon revealed a type-II isotherm with a type-H4 hysteresis (Fig. 5).

Type-II isotherms are characteristic of multilayer adsorption on non-porous or macroporous solids.[50] Non-graphitized carbons can produce smooth type-II isotherms, although synthesis

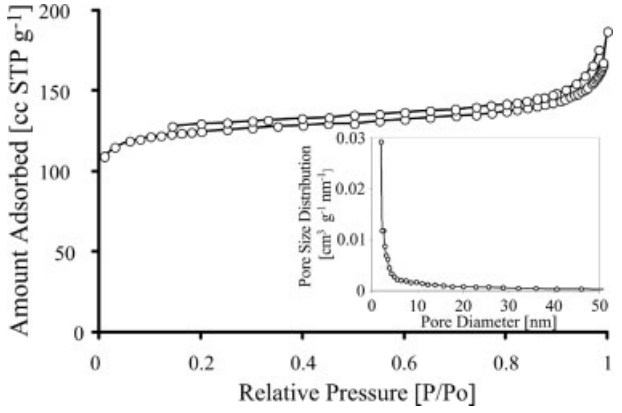

Figure 5. Nitrogen-sorption isotherm and adsorption-branch pore size distribution (inset) of 3DOM RF carbon monoliths.

and processing conditions play a deciding role in the resulting porosity of such products.[51–53] While type-IV isotherms have been observed for phenolic resin carbon aerogels that were templated with polymer[54] and silica[55] colloids, MCM-48 mesoporous silica,[56] and cetyltrimethylammonium bromide (CTAB) sufactant,[57] respectively, only macroporous templates were employed in our syntheses. In this case, a type-II isotherm could signify the collapse or closure of mesopores in the RF gel via the loss of solvent during thermal processing. The pore size distribution revealed the presence of some mesoporosity with increasing intensity near the micropore regime. The absence of a type-IV isotherm and the low intensity of the mesopore size distribution suggest that mesopores in 3DOM RF carbon may contribute weakly to the sorption of N_2 molecules. A Brunauer–Emmett–Teller (BET) specific surface area of 326 $m^2 g^{-1}$ was calculated from the N_2-adsorption data. Microporosity was determined to be a large component of the surface area (196 $m^2 g^{-1}$) as estimated by a *t*-plot. Type-H4 isotherm hysteresis have been associated with slit-shaped microporosity,[50] and micropores are thought to exist between the randomly arranged graphene sheets in hard carbons.[41,58–60]

Elemental analysis (EA) revealed appreciable amounts of H and O within 3DOM carbon. EA [wt.-%]: C (87.4±0.5), H (1.0±0.1), N (0.3±0.1), and O (8.0±0.6). The presence of other elements is known to strongly influence the electrochemical properties of carbon. For example, hydrogen-containing carbons have relatively large specific capacities (ca. 600–1000 mA h g^{-1}),[33,61] although they exhibit poor cycling performance[34] and larger cycling hystereses.[35] They typically contain an atomic ratio of ca. 0.2 H/C, which is similar to the elemental composition of the 3DOM carbon products reported here.[33,47] Significant amounts of oxygen (>5 wt.-%) have also been reported to increase cycling hysteresis in carbon electrodes.[62] This elemental analysis data corresponds well with the Fourier-transform infrared (FT-IR) spectrum of 3DOM carbon (Fig. 6a). Evidence of carbon–hydrogen bonding was not detected, although carbon–oxygen linkages consistent with C=O vibration (1711 cm^{-1}), conjugated carbonyl systems (1575 cm^{-1}), and ether-like vibrations in phenolic materials (ca. 1260–1000 cm^{-1}) were observed.[63]

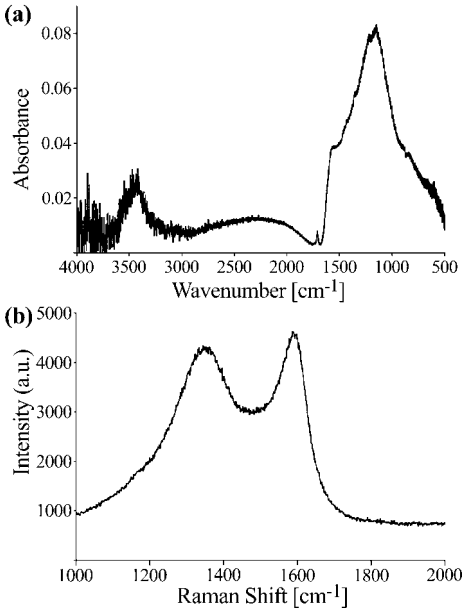

Figure 6. a) FTIR and b) Raman spectra of 3DOM carbon monoliths.

Raman spectra of 3DOM RF carbons displayed broad bands at 1350 cm^{-1} and 1587 cm^{-1}, which are characteristic of a symmetry breakdown at the edge of graphene sheets (D band) and the E_{2g} vibrational mode of graphite layers (G band), respectively (Fig. 6b). These bands are exhibited by various types of carbon,[64–67] and have been reported in two studies of RF carbons.[47,51] The presence of both D and G bands is consistent with the model of turbostratically disordered graphene sheets contained in hard carbons. The D band was red-shifted at higher laser excitation wavelength (1096 nm) (data not shown), in

ADVANCED FUNCTIONAL MATERIALS

agreement with observations by McCreery et al.[65] The D/G intensity ratio was ca. 47–55 %, which is comparable to values reported for glassy carbon.

3DOM carbon exhibited reasonable electrical conductivity (0.22 S cm^{-1}), even though the material was highly porous, because the walls were well-interconnected in three dimensions. Larger values have been reported for RF carbon mesoporous foam[54] and aerogels,[51,68,69] since electrical conductivity is inversely proportional to pore volume. Still, the electrical conductivity of 3DOM carbon is similar to that reported by Tanaka and co-workers,[43,44] and is considered sufficient for use in Li-ion batteries.

The ionic conductivity of electrolyte in the 3DOM carbon matrix was measured from the complex impedance spectrum shown in Figure 7 and compared with that of the pure electrolyte. The bulk ionic conductivity of 1 M $LiPF_6$ in a 1:1 (v/v) mixture of ethylene carbonate (EC) and diethyl carbonate (DEC) from

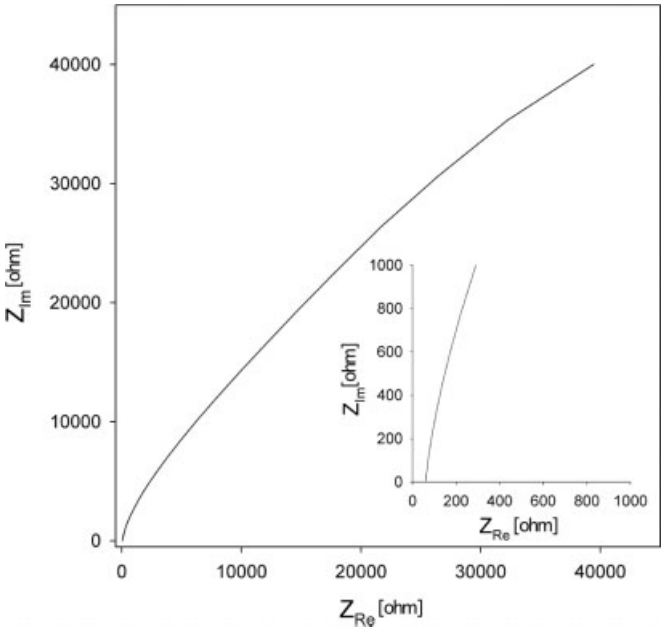

Figure 7. Alternating current (AC) impedance spectrum obtained with 1 M $LiPF_6$ dissolved in EC+DEC (1:1, vol./vol.) in a 3DOM carbon matrix. The inset is a magnified plot that shows the intercept with the real impedance axis.

EM Industries is quoted to be 7.3–8.3 mS cm^{-1}. The ionic conductivity of the electrolyte-filled 3DOM carbon was 4.8 mS cm^{-1}. Even though the ionic conductivity decreased when the electrolyte was infiltrated in the macroporous matrix, the extent of decrease was relatively small, suggesting that movement of lithium ions in the electrolyte was virtually unobstructed by the three-dimensionally interconnected pore structure.

2.2. Rate Performance of 3DOM Carbon

Galvanostatic charge–discharge experiments were performed to evaluate the rate performance of 3DOM carbon in comparison with a bulk carbon monolith synthesized by an identical method but without the use of a template, and with an electrode assembled from RF carbon spheres (diameters: 104 ± 17 nm, Fig. 8).

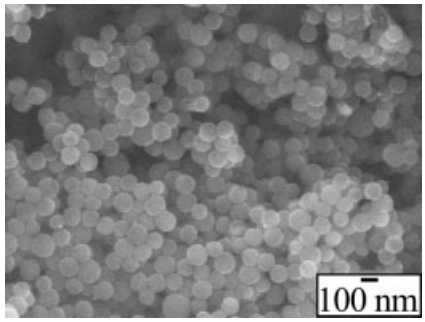

Figure 8. SEM image of spherical carbon.

In contrast with the 3DOM carbon monoliths, the carbon sphere electrode required a binder. 3DOM carbon samples with two different pore sizes (C1 and C2) were studied to determine reproducibility and the effect of macropore size on rate performance. Figure 9a shows charge–discharge profiles of 3DOM carbon samples C1 and C2, as well as of non-templated and spherical carbon electrodes. The specific current used for electrodes C1, C2, and the spherical carbon electrode was 15.2 mA g^{-1} and that used for the non-templated carbon electrode was 1.5 mA g^{-1}. When a specific current of 15.2 mA g^{-1} was applied to the C1 electrode, a specific discharge capacity of 299 mA h g^{-1} was determined. The specific capacity decreased by 50 % upon a ten-fold increase in specific current. Large irreversible capacities were observed for all samples, accounting for as much as two-thirds of the initial charging capacities. These instances were likely due to SEI layer formation and the inherent nature of hard carbon. The magnitudes of the irreversible capacities of 3DOM and spherical carbons were greater than for non-3DOM carbon, since the former have larger surface areas available for SEI layer growth.

Although phenolic resin carbons have been reported with reversible gravimetric capacities of ca. 500 mA h g^{-1},[45] 3DOM RF carbons exhibited reversible discharge capacities lower than those for commercial graphitic anode materials. Electrode thickness may contribute to this apparent deficiency. Many studies report electrodes tens of micrometers in thickness, but the samples reported here are thicker than 400 μm. In general, capacity decreases with increasing electrode thickness, due to larger electrical and electrochemical resistivities. Furthermore, significant amounts of capacity may have been overlooked due to the constant current cycling method employed in this study, which applied a reducing current to the carbon until a potential of 0 V was achieved. Hard carbons have been shown to possess low voltage plateaus that extend to relatively large capacities.[33] A constant voltage segment at ca. 0 V could have more fully charged the carbon at its low-voltage plateau until little or

no current was passed. This will be done in future experiments to gain larger specific capacities.

The rate performance of the larger-pore C2 electrode was similar to that of the C1 electrode (Fig. 9b). The two electrode thicknesses were designed to be similar (Table 1), so that thickness effects on rate performance could be ignored. The data indicated that the rate performance of 3DOM carbon was not

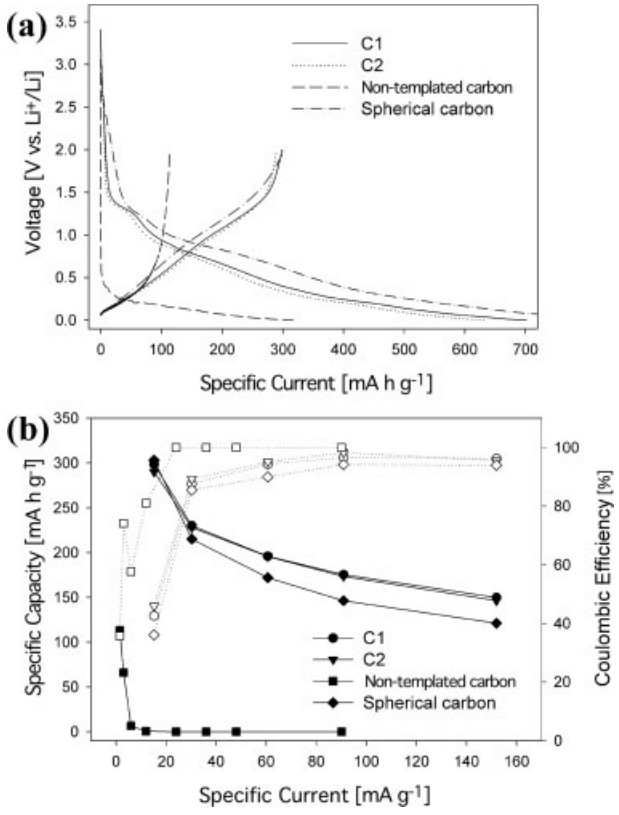

Figure 9. a) Charge–discharge profiles of C1 (solid line), C2 (dotted line), non-templated carbon (dashed line), and spherical carbon (dashed-dotted line). Specific currents were 15.2 mA g^{-1} (C1, C2, spherical carbon) and 1.5 mA g^{-1} (non-templated carbon). b) Rate performances and coulombic efficiencies of these samples. Open symbols refer to coulombic efficiencies and filled symbols to specific capacities.

significantly affected by pore size within the pore-size range studied, because both samples had identical wall thicknesses (ca. 10 nm) which provided short diffusion lengths. On the other hand, non-templated carbon (thickness: 496 μm, surface area <1 m^2 g^{-1})[57] did not show any significant capacities at specific currents greater than 12 mA g^{-1} (Fig. 9b). This implies that, as expected for a rate-limiting diffusion process, the nanoscale lithium-ion diffusion lengths improved rate capabilities. The spherical carbon electrode exhibited slightly higher specific capacity than 3DOM carbon at slow rates. However, as the specific current was increased, the more open 3DOM structure with its thinner walls performed better than the spherical carbon sample.

The coulombic efficiencies of C1 and C2 were 43 and 46 % for the first cycle, but were greater than 90 % for subsequent cycles. The low coulombic efficiencies in the first cycle were likely due to SEI layer formation on the relatively large specific surface of the sample (326 m^2 g^{-1}).

2.3. 3DOM Carbon Coated with SnO_2 Nanoparticles

3DOM carbon has high porosity and therefore low volumetric energy density. However, one can envision an improvement by coating the 3DOM carbon surface with a uniform layer of SnO_2, which has a larger theoretical specific capacity (780 mA h g^{-1}) than carbon, while maintaining an accessible pore structure. Since it was important to avoid pore blockage during coating, we opted for an aqueous salt-imbibition process, in which $SnSO_4$ was first deposited on the surface of 3DOM carbon from an acidic solution and subsequently converted to SnO_2 by heating at 400 °C for 2 h under nitrogen. In the first step, 20–30 nm sized tin sulfate nanoparticles formed on the macropore walls (Fig. 10a). Carbon, oxygen, sulphur, and tin were observed for the $SnSO_4$-imbibed 3DOM carbon sample by energy-dispersive X-ray spectroscopy (EDS) (Fig. 11), confirming that the observed nanoparticles on the surface were composed of tin sulfate. The conversion reaction in the second step proceeded by the following thermal decomposition:[70]

$$SnSO_4\,(s) \rightarrow SnO_2\,(s) + SO_2\,(g) \quad (1)$$

The resulting SnO_2 particles homogeneously covered the surface of 3DOM carbon (Fig. 10b) and had sizes between 10–40 nm. As a consequence, the estimated wall thickness increased from 10 to 27 nm. The powder X-ray microdiffraction pattern of this composite showed only reflections for SnO_2 (powder diffraction file (PDF)# 41-1445), even though a small sulfur peak remained in the EDS spectrum (Fig. 11). Minor amounts of unreacted $SnSO_4$ may have been present as very fine particles, whose XRD peaks were broadened to the extent that they were not detected. Nonetheless, the relative intensities of the sulfur and oxygen peaks were significantly reduced in the converted sample, consistent with the loss of SO_2 during formation of SnO_2. The SnO_2 content of the SnO_2-coated 3DOM carbon sample (from SnO_2 and $SnSO_4$) was measured to be 10 wt.-% by thermogravimetric analysis (TGA).

When the product shown in Figure 10b was heated in air from 25 °C to 900 °C at a rate of 10 °C min^{-1}, carbon from the original SnO_2/C composite was combusted, leaving a tin oxide skeleton, whose SEM image is provided in Figure 10d. Approximately 10–20 nm sized tin oxide particles were aggregated and some parts (ca. 30 %) of the 3DOM structure were maintained. This provides further confirmation that a nanometer-sized tin oxide coating had formed on the 3DOM carbon sample in Figure 10b.

ADVANCED FUNCTIONAL MATERIALS

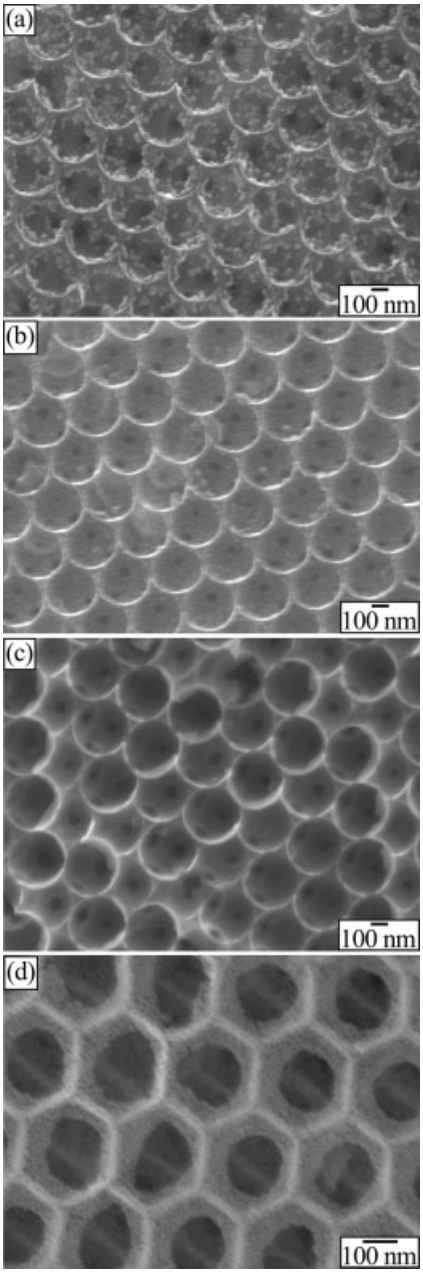

Figure 10. SEM images of a) precipitated tin sulfate nanoparticles on the surface of 3DOM carbon; b) tin oxide-nanoparticle-coated 3DOM carbon prepared by thermal decomposition of tin sulfate at 400 °C; c) the sample shown in (b) after thirty electrochemical cycles; and d) 3DOM tin oxide obtained after heating of the sample shown in (a) at 900 °C in air.

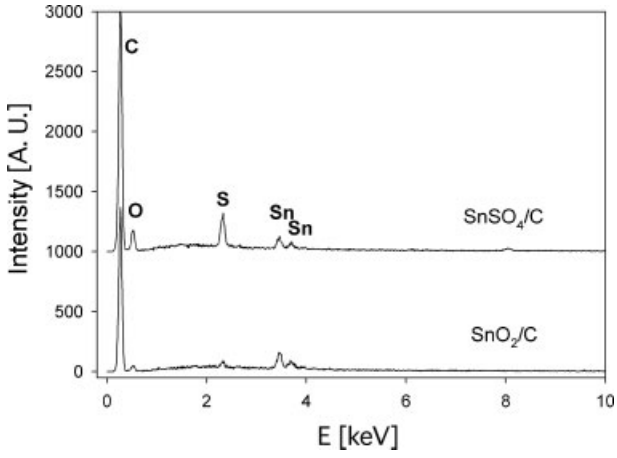

Figure 11. EDS spectra of the precipitated tin sulfate nanoparticles on the surface of 3DOM carbon ($SnSO_4$/C) and tin oxide nanoparticle-coated 3DOM carbon (SnO_2/C).

2.4. Electrochemical Characteristics of SnO_2-Coated 3DOM Carbon

Galvanostatic charge–discharge experiments were performed to compare cycle performance of a SnO_2-coated 3DOM carbon electrode (sample SnC1, 888 μm thick) with an unmodified 3DOM carbon electrode of similar thickness (sample C3, 751 μm thick). A constant specific current of 40 mA g^{-1} was applied within a voltage range of 0.0–2.0 V (vs. Li/Li^+) over thirty cycles. The specific discharge capacity of the SnC1 electrode (278 mA h g^{-1}) was 55 mA h g^{-1} higher than that of the C3 electrode (223 mA h g^{-1}). However, with additional cycles, the specific capacity of the SnC1 electrode decreased and was nearly identical to that of the C3 electrode by the thirtieth cycle (Fig. 12a). In comparison, 3DOM carbon showed a more stable cycle performance. The decrease in discharge capacity of SnO_2-coated 3DOM carbon is believed to be due to detachment of lithiated tin oxide nanoparticles by volume changes during charge and discharge. The SEM image of the cycled material (Fig. 10c) shows less surface texture than the image of the fresh material (Fig. 10b), indicating that SnO_2 loss had occurred. Yet the periodic structure of the 3DOM carbon support was maintained after thirty cycles.

To compare the rate performance of SnO_2-coated 3DOM carbon (SnC2) with that of 3DOM carbon (C1), cells were tested for four cycles with a higher specific current during each subsequent cycle. Specific capacities obtained at increasing specific currents are shown in Figure 12b. When a specific current of 15.2 mA g^{-1} was applied to the SnC2 electrode, its specific capacity was 348 mA h g^{-1}, i.e., 49 mA h g^{-1} larger than that of the C1 electrode (Fig. 12b). When the specific current was increased from 15.2 to 90.9 mA g^{-1}, the discharge capacities of the SnC2 and C1 electrodes decreased to 58 % and 50 % of the initial capacities, respectively. Overall, the rate performance of SnO_2-coated 3DOM carbon was better than that of 3DOM carbon.

3. Conclusion

3DOM carbon was synthesized via colloidal-crystal templating of an RF sol. In an application as an anode for lithium-ion secondary batteries, 3DOM carbon has several advantages that would permit high rate performance of lithium-ion secondary batteries: 1) nanometer-sized solid-state diffusion lengths, 2) high ionic conductivity of the electrolyte in the porous ma-

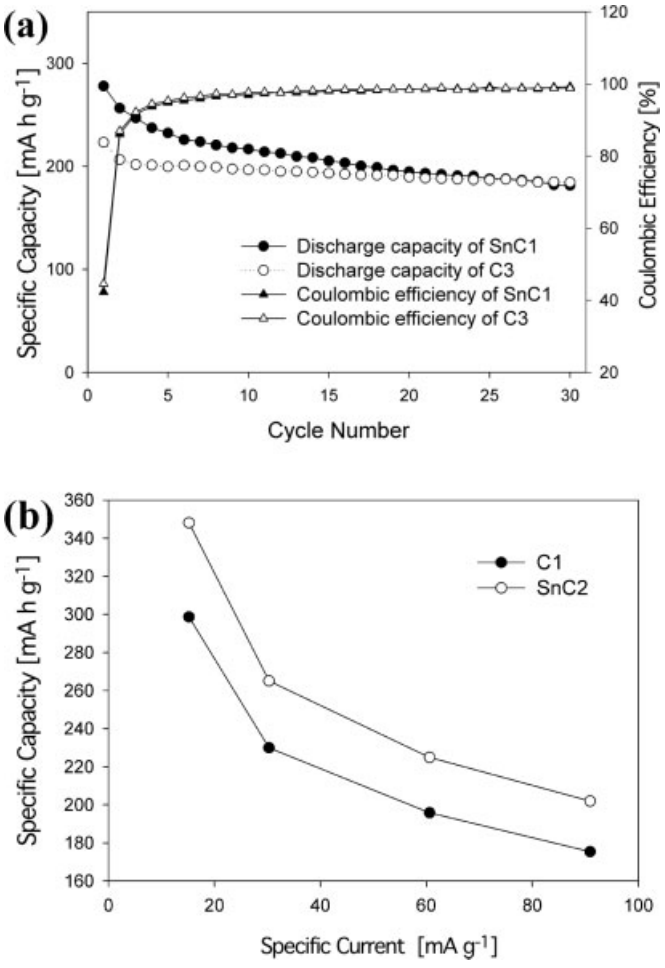

Figure 12. a) Cycle performance and coulombic efficiencies of SnC1 and C3 electrodes at a specific current of 40 mA g^{-1}, and b) rate performance of SnC2 and C1 electrodes over multiple specific currents.

trix, and 3) reasonable electric conductivity. These advantages arise from the morphology of 3DOM materials which have well-interconnected wall and pore structures and nanoscale wall thicknesses. As a result, rate performance was significantly enhanced compared to similarly prepared non-templated carbon and was also improved compared to spherical carbon electrodes mixed with binder. It was, however, not affected by the pore spacing in the range from approximately 300 to 350 nm, mainly because wall thicknesses were similar in these materials and the pore sizes were significantly larger than mobile species in the electrochemical system. 3DOM carbon retained three orders of magnitude greater discharge capacity than bulk carbon at specific currents greater than 12 mA g^{-1}, and possessed good cycling stability with 83 % reversible capacity retention after thirty cycles. The specific capacity of 3DOM carbon could be increased by coating the carbon surface with tin oxide nanoparticles. Rate performance also increased for the coated sample. However, the discharge capacities of SnO_2-coated 3DOM carbon decreased after repeated cycling, because of detachment of lithium–tin alloy nanoparticles by volume changes during charge–discharge processes. All RF carbons studied here exhibited reversible capacities less than that of graphite, large irreversible capacities, and cycling hysteresis ≥ 1 V, which were inherent to the hard carbon used in these experiments. Regardless, the purpose of our work was not to find nor to optimize an ideal form of carbon, which was a factor limited by our synthetic approach. Rather, it was to study the effect of the inverse-opal geometry on the electrochemical properties of carbon monoliths, which yielded positive indications that the inverse-opal geometry is capable of high-rate performance. The ability to prepare monolithic pieces of 3DOM carbon facilitates its handling and testing as anode material, so that it can be prepared as a stand-alone electrode or as a platform for three-dimensionally microstructured batteries.[71,72] The open architecture allows further modification of the electrode, which can be advantageous for battery applications, as well as sensing applications.

4. Experimental

Materials and Synthesis: Monodisperse poly(methyl methacrylate) (PMMA) spheres were synthesized via an emulsifier-free emulsion-polymerization technique and packed into colloidal crystals by gravitational settling [73]. Resorcinol-formaldehyde (RF) polymer was used as a source of active carbon [57,74]. To prepare monolithic macroporous carbon, PMMA colloidal-crystal pieces with a cross-sectional area of ca. 1 cm^2 and a thickness of ca. 5 mm were soaked in RF solution with a composition of resorcinol (99 + %, A.C.S. reagent, Sigma–Aldrich)/ formaldehyde (U.S.P. 37 % aq. solution)/sodium carbonate (as catalyst, Fisher)/deionized water in a 1:2:0.02:5.68 molar ratio. Vacuum was applied to aid infiltration of the mixture into the template. After infiltration and removal of the monolith from the RF solution, excess solution covering the outside of the monolith was carefully wiped off with tissue paper. The template–RF-sol composite was aged in a sealed polyethylene bottle at 85 °C for three days and then dried in a convection oven at 85 °C with the lid open. The RF gel was carbonized at 900 °C for 2 h under a flowing nitrogen atmosphere using a heating ramp of 5 °C min^{-1}, and PMMA spheres were removed by thermal decomposition during this process. The monolithic 3DOM carbon pieces were polished with 600-grit sandpaper to eliminate non-porous regions covering the outside of the monolithic pieces and to control the thickness of the electrodes (see Table 1 for thicknesses). The polished pieces were cleaned by multiple sonication steps in water at room temperature until the water remained clear. They were then dried overnight in a convection oven at 85 °C. Non-templated monolithic carbon was synthesized via the same RF sol–gel process, except that no PMMA template was used.

For the synthesis of SnO_2-coated samples, monolithic 3DOM carbon pieces were soaked in an aqueous tin sulfate solution under vacuum and then sonicated for 5 h. The composition of the solution was $SnSO_4$/H_2SO_4/H_2O in a 1:1.8:277 molar ratio. After soaking, excess solution covering the outside of 3DOM carbon pieces was removed by wiping with a paper tissue, and the samples were dried overnight at room temperature. Subsequently, they were heated at 400 °C for 2 h under a nitrogen atmosphere to decompose $SnSO_4$ (s) into SnO_2 (s) and SO_2 (g) [70].

Submicrometer-sized spherical carbon was synthesized through RF polymerization with an emulsifier [8]. A mixture of resorcinol (3 mmol), formaldehyde (3 mol), sodium carbonate (0.042 mmol), cetyltrimethylammonium bromide (CTAB, 0.738 mmol), and deionized water (16.8 mol) was stirred to obtain surfactant-stabilized RF sols. The RF sol was then polymerized at 85 °C for three days. After drying, the product was heat-treated at 900 °C for 2 h under nitrogen with a heating rate of 5 °C min^{-1} to carbonize the RF polymer.

Characterization of Materials: Scanning electron microscope (SEM) images were obtained on a JEOL JSM-6500 SEM operating at 5 kV.

ADVANCED FUNCTIONAL MATERIALS

Uncoated samples were used for imaging, except for the PMMA sample (shown in Fig. 2a), which was coated with 7 nm of Pt. Energy-dispersive X-ray spectroscopy (EDS) was used to analyze the atomic composition of 3DOM carbon materials modified with tin sulfate or tin oxide. C, H, N, and O elemental analyses (EAs) of 3DOM carbon were performed by Atlantic Microlab Inc. of Norcross, GA. Nitrogen-sorption measurements were done on a Micromeritics ASAP 2000 gas sorptometer. Specific surface areas were calculated by the Brunauer–Emmett–Teller (BET) method, and pore sizes and volumes were estimated from pore size distributions using from the adsorption branch of the isotherm. The surface area contribution of micropores was calculated from a *t*-plot. Thermogravimetric analysis (TGA) was performed on a Netzsch-STA 409 PC thermal analyzer to measure the SnO_2 content of SnO_2-coated macroporous carbon electrodes; the samples were heated in alumina crucibles under airflow to 900 °C at 10 °C min^{-1}. A diffuse-reflectance UV-vis spectrum of 3DOM carbon was obtained on a Spectral Instruments spectrophotometer Model 440 using a fiber-optic reflectance probe and a tungsten lamp. The spectrum was referenced against a white $BaSO_4$ standard. Powder X-ray diffraction (XRD) patterns of 3DOM carbon were obtained on a Bruker AXS D8 Advance diffractometer with Cu $K\alpha$ radiation generated at 40 kV and 40 mA. Microdiffraction studies of SnO_2-coated 3DOM carbon were obtained on a Bruker AXS microdiffractometer. Raman spectroscopy was performed with a LabRam HR spectrometer (Jobin-Yvon Co., France) with a 514.532 nm Ar-ion laser operating at 1 mW. Signals were collected by a multichannel charge-coupled device (CCD) detector maintained at 77 K. The instrument was calibrated using the emission lines of a Ne lamp. Data was acquired from a polished 3DOM carbon monolith that was mounted on a glass microscope slide. A total of two scans were collected using an acquisition time of 60 s per scan. Fourier-transform infrared (FTIR) spectroscopy was done on a Nicolet Magna-IR 760 spectrometer. Spectra were obtained in the mid-IR using FTIR-grade KBr pellets.

Electrochemical Characterization: The galvanostatic charge–discharge measurements were performed with a two-electrode cell (Fig. 4), in which a monolithic 3DOM carbon, monolithic non-templated carbon or a spherical carbon electrode were used as the working electrode, and Li-metal foil as the counter- and reference electrodes. This electrode assembly was constructed in a dry room with < 1 % relative humidity, and was contained in a three-necked glass round-bottomed flask. The flask was sealed with electrodes connected to their respective contacts with alligator clips. The electrolyte was 1.0 M $LiPF_6$ dissolved in a mixture of ethylene carbonate and diethyl carbonate (1:1 vol./vol.) (LP40 Selectipur battery electrolyte from EM Industries Inc.). The separator (Celgard 2400, microporous polypropylene membrane) was purchased from Celgard Inc. For the preparation of cells, monolithic 3DOM carbon and non-templated carbon pieces were fixed on a piece of copper foil. These electrodes were made without any conducting agent or binder. In case of the electrode prepared from spherical carbon, a slurry made with active material and poly(vinylidene fluoride) (10:1.5 wt./wt.) was coated on copper foil. The electrodes were dried under vacuum for 12 h at 100 °C before use.

Galvanostatic cycling experiments were conducted with an Arbin battery-testing system. For these experiments, various gravimetric currents were applied within a voltage range of 0.0–2.0 V (vs. Li/Li$^+$). Specific currents were increased from 15.2 to 152 mA g^{-1} as the cycle number increased. The electrical conductivity of monolithic macroporous carbon was measured through the van der Pauw method with four probes attached to the sample using colloidal graphite as an adhesive (Ted Pella Inc., colloidal graphite with isopropanol) [75]. Measurements were performed at room temperature.

The ionic conductivity of the electrolyte was measured by complex impedance analysis using a Solartron 1260 frequency-response analyzer in the frequency range of 1.0 Hz–1.0 MHz. For these measurements, a cell was assembled by sandwiching 3DOM carbon infiltrated with $LiPF_6$/EC+DEC electrolyte between two sets of separators and Cu foils (configuration: glass slide/Cu foil/separator/electrolyte-infiltrated 3DOM carbon/separator/Cu foil/glass slide, all clipped together). An alternating current (AC) perturbation of 10 mV was applied to the cell. The electrolyte resistance was determined from the high frequency intercept of the impedance spectrum with the real axis and converted first to resistivity by normalizing resistance to the area and thickness of electrolyte-infiltrated monolithic 3DOM carbon, and then to ionic conductivity, the reciprocal of ionic resistivity [76,77].

Received: May 1, 2004
Final version: September 14, 2004

[1] B. B. Owens, W. H. Smyrl, J. J. Xu, *J. Power Sources* **1999**, *81–82*, 150.
[2] Y. Idota, T. Kubota, A. Matsufuji, Y. Maekawa, T. Miyasaka, *Science* **1997**, *276*, 1395.
[3] M. Winter, J. O. Besenhard, M. E. Spahr, P. Novak, *Adv. Mater.* **1998**, *10*, 725.
[4] H. Li, L. Shi, W. Lu, X. Huang, L. Chenz, *J. Electrochem. Soc.* **2001**, *148*, A915.
[5] L. Y. Beaulieu, T. D. Hatchard, A. Bonakdarpour, M. D. Fleischauer, J. R. Dahn, *J. Electrochem. Soc.* **2003**, *150*, A1457.
[6] L. M. L. Fransson, J. T. Vaughey, K. Edstrom, M. M. Thackeray, *J. Electrochem. Soc.* **2003**, *150*, A86.
[7] J. Graetz, C. C. Ahn, R. Yazami, B. Fultz, *Electrochem. Solid-State Lett.* **2003**, *6*, A194.
[8] K. T. Lee, Y. S. Jung, S. M. Oh, *J. Am. Chem. Soc.* **2003**, *125*, 5652.
[9] J. P. Maranchi, A. F. Hepp, P. N. Kumtaa, *Electrochem. Solid-State Lett.* **2003**, *6*, A198.
[10] C. J. Patrissi, C. R. Martin, *J. Electrochem. Soc.* **1999**, *146*, 3176.
[11] B. B. Owens, S. Passerini, W. H. Smyrl, *Electrochim. Acta* **1999**, *45*, 215.
[12] P. Poizot, S. Laruelle, S. Grugeon, L. Dupont, J. M. Tarascon, *Nature* **2000**, *407*, 496.
[13] S. Nordlinder, K. Edstrom, T. Gustafsson, *Electrochem. Solid-State Lett.* **2001**, *4*, A129.
[14] H. Huang, S. C. Yin, T. Kerr, N. Taylor, L. F. Nazar, *Adv. Mater.* **2002**, *14*, 1525.
[15] S. C. Mui, P. E. Trapa, B. Huang, P. P. Soo, M. I. Lozow, T. C. Wang, R. E. Cohen, A. N. Mansour, S. Mukerjee, A. M. Mayes, D. R. Sadoway, *J. Electrochem. Soc.* **2002**, *149*, A1610.
[16] J. S. Sakamoto, B. Dunn, *J. Mater. Chem.* **2002**, *12*, 2859.
[17] N. Li, D. T. Mitchell, K. P. Lee, C. R. Martin, *J. Electrochem. Soc.* **2003**, *150*, A979.
[18] H. Yan, S. Sokolov, J. C. Lytle, A. Stein, F. Zhang, W. H. Smyrl, *J. Electrochem. Soc.* **2003**, *150*, A1102.
[19] F. Sauvage, E. Baudrin, M. Morcrette, J. M. Tarascon, *Electrochem. Solid-State Lett.* **2004**, *7*, A15.
[20] M. D. Levi, D. Aurbach, *J. Phys. Chem. B* **1997**, *101*, 4641.
[21] M. Nishizawa, R. Hashitani, T. Itoh, T. Matsue, I. Uchida, *Electrochem. Solid-State Lett.* **1998**, *1*, 10.
[22] D. Larcher, C. Masquelier, D. Bonnin, Y. Chabre, V. Masson, J. B. Leriche, J. M. Tarascon, *J. Electrochem. Soc.* **2003**, *150*, A133.
[23] K. Nakahara, R. Nakajima, T. Matsushima, H. Majima, *J. Power Sources* **2003**, *117*, 131.
[24] C. J. Curtis, J. Wang, D. L. Schulz, *J. Electrochem. Soc.* **2004**, *151*, A590.
[25] A. J. Bard, L. R. Faulkner, *Electrochemical Methods: Fundamentals and Applications*, John Wiley & Sons, New York **1980**.
[26] J. P. Meyers, M. Doyle, R. M. Darling, J. Newman, *J. Electrochem. Soc.* **2000**, *147*, 2930.
[27] A. Stein, R. C. Schroden, *Curr. Opin. Solid State Mater. Sci.* **2001**, *5*, 553.
[28] A. A. Zakhidov, R. H. Baughman, Z. Iqbal, C. Cui, I. Khayrullin, S. O. Dantas, J. Marti, V. G. Ralchenko, *Science* **1998**, *282*, 897.
[29] R. W. J. Scott, S. M. Yang, D. E. Williams, G. A. Ozin, *Chem. Commun.* **2003**, 688.
[30] J. C. Lytle, H. Yan, N. Ergang, W. H. Smyrl, A. Stein, *J. Mater. Chem.* **2004**, *14*, 1616.

[31] B. T. Holland, C. F. Blanford, T. Do, A. Stein, *Chem. Mater.* **1999**, *11*, 795.
[32] H. Yan, C. F. Blanford, B. T. Holland, W. H. Smyrl, A. Stein, *Chem. Mater.* **2000**, *12*, 1134.
[33] J. R. Dahn, T. Zheng, Y. Liu, J. S. Xue, *Science* **1995**, *270*, 590.
[34] T. Zheng, Y. Liu, E. W. Fuller, S. Tseng, U. von Sacken, J. R. Dahn, *J. Electrochem. Soc.* **1995**, *142*, 2581.
[35] T. Zheng, W. R. McKinnon, J. R. Dahn, *J. Electrochem. Soc.* **1996**, *143*, 2137.
[36] J. R. Dahn, A. K. Sleigh, H. Shi, J. N. Reimers, Q. Zhong, B. M. Way, *Electrochim. Acta* **1993**, *38*, 1179.
[37] N. Deprez, D. S. McLachlan, *J. Phys. D* **1988**, *21*, 101.
[38] C. Oloman, M. Matte, C. Lum, *J. Electrochem. Soc.* **1991**, *138*, 2330.
[39] A. Celzard, J. F. Mareche, G. Furdin, S. Puricelli, *J. Phys. D* **2000**, *33*, 3094.
[40] C.-W. Wang, Y.-W. Yi, A. M. Sastry, J. Shim, K. A. Striebel, *J. Electrochem. Soc.* **2004**, *151*, A1489.
[41] E. Buiel, J. R. Dahn, *Electrochim. Acta* **1999**, *45*, 121.
[42] K. Ouchi, H. Honda, *Fuel* **1959**, *38*, 429.
[43] K. Tanaka, K. Ohzeki, T. Yamabe, S. Yata, *Synth. Met.* **1984**, *9*, 41.
[44] S. Yata, H. Kinoshita, M. Komori, N. Ando, T. Kashiwamura, T. Harada, K. Tanaka, T. Yamabe, *Synth. Met.* **1994**, *62*, 153.
[45] T. Zheng, Q. Zhong, J. R. Dahn, *J. Electrochem. Soc.* **1995**, *142*, L211.
[46] S. A. Al-Muhtaseb, J. A. Ritter, *Adv. Mater.* **2003**, *15*, 101.
[47] N. Kishore, S. Sachan, K. N. Rai, A. Kumar, *Carbon* **2003**, *41*, 2961.
[48] R. C. Schroden, N. Balakrishnan, *Inverse Opal Photonic Crystals—A Laboratory Guide* (http://www.mrsec.umn.edu/mrsec/learningmodule-library.html), University of Minnesota MRSEC, Minneapolis, MN **2001**.
[49] R. C. Schroden, M. Al-Daous, C. F. Blanford, A. Stein, *Chem. Mater.* **2002**, *14*, 3305.
[50] F. Rouquerol, J. Rouquerol, K. Sing, *Adsorption by Powders and Porous Solids: Principles, Methodology, Applications*, Academic Press, New York **1999**.
[51] A. W. P. Fung, Z. H. Wang, K. Lu, M. S. Dresselhaus, R. W. Pekala, *J. Mater. Res.* **1993**, *8*, 1875.
[52] S. Q. Zhang, J. Wang, Z. S. Zhen, Z. Q. Deng, B. Lai, S. M. Zhou, A. Chen, L. Y. Chen, *Nanostruct. Mater.* **1999**, *11*, 375.
[53] T. Horikawa, J. Hayashi, K. Muroyama, *Carbon* **2004**, *42*, 1625.
[54] W. W. Lukens, G. D. Stucky, *Chem. Mater.* **2002**, *14*, 1665.
[55] S. Han, T. Hyeon, *Chem. Commun.* **1999**, 1955.
[56] R. Ryoo, S. H. Joo, S. Jun, *J. Phys. Chem. B* **1999**, *103*, 7743.
[57] K. T. Lee, S. M. Oh, *Chem. Commun.* **2002**, 2722.
[58] W. Xing, J. S. Xue, T. Zheng, A. Gibaud, J. R. Dahn, *J. Electrochem. Soc.* **1996**, *143*, 3482.
[59] E. Buiel, A. E. George, J. R. Dahn, *J. Electrochem. Soc.* **1998**, *145*, 2252.
[60] E. Buiel, A. E. George, J. R. Dahn, *Carbon* **1999**, *37*, 1399.
[61] P. Papenek, M. Radosavljevic, J. E. Fischer, *Chem. Mater.* **1996**, *8*, 1519.
[62] E. Frackowiak, F. Beguin, *Carbon* **2002**, *40*, 1175.
[63] S. Biniak, A. Swiatkowski, M. Pakula, in *Active Carbon-Electrolyte Interfaces*, Vol. 27 (Ed: L. R. Radovic), Marcel Dekker, New York **2001**, Ch. 3.
[64] F. Tuinstra, J. Koenig, *J. Chem. Phys.* **1970**, *53*, 1126.
[65] Y. Wang, D. C. Alsmeyer, R. L. McCreery, *Chem. Mater.* **1990**, *2*, 557.
[66] J. Schwan, S. Ulrich, V. Batori, H. Ehrhardt, *J. Appl. Phys.* **1996**, *80*, 440.
[67] K. Ray, III, R. L. McCreery, *Anal. Chem.* **1997**, *69*, 4680.
[68] R. Saliger, V. Bock, R. Petricevic, T. Tillotson, S. Geis, J. Fricke, *J. Non-Cryst. Solids* **1997**, *221*, 144.
[69] J. Wang, S. Q. Zhang, Y. Z. Guo, J. Shen, S. M. Attia, B. Zhou, G. Z. Zheng, Y. S. Gui, *J. Electrochem. Soc.* **2001**, *148*, D75.
[70] J. Cueilleron, O. Hartmanshenn, *Bull. Soc. Chim. Fr.* **1959**, 168.
[71] R. W. Hart, H. S. White, B. Dunn, D. R. Rolison, *Electrochem. Commun.* **2003**, *5*, 120.
[72] J. W. Long, B. Dunn, D. R. Rolison, H. S. White, *Chem. Rev.* **2004**, *104*, 4463.
[73] D. Zou, S. Ma, R. Guan, M. Park, L. Sun, J. J. Aklonis, R. Salovey, *J. Polym. Sci., Polym. Chem. Ed.* **1992**, *30*, 137.
[74] R. W. Pekala, *J. Mater. Sci.* **1989**, *24*, 3221.
[75] L. J. van der Pauw, *Philips Tech. Rev.* **1958/59**, *20*, 220.
[76] G. B. Appetecchi, W. Henderson, P. Villano, M. Berrettoni, S. Passerini, *J. Electrochem. Soc.* **2001**, *148*, A1171.
[77] M. K. Song, Y. T. Kim, Y. T. Kim, B. W. Cho, B. N. Popov, H. W. Rhee, *J. Electrochem. Soc.* **2003**, *150*, A439.

